Research Article

Nano Research
2021, 14(4): 1126–1134

ISSN 1998-0124 CN 11-5974/O4
https://doi.org/10.1007/s12274-020-3161-6

Colloidal lead-free $Cs_2AgBiBr_6$ double perovskite nanocrystals: Synthesis, uniform thin-film fabrication, and application in solution-processed solar cells

Razi Ahmad[1,5], Gautam Virender Nutan[1], Dinesh Singh[2], Govind Gupta[1], Udit Soni[3], Sameer Sapra[4], and Ritu Srivastava[1] (✉)

[1] *Advanced Materials and Devices Metrology Division, CSIR-National Physical Laboratory, Dr. K.S. Krishnan Road, New Delhi-110012, India*
[2] *Indian Reference Materials Division, CSIR-National Physical Laboratory, Dr. K.S. Krishnan Road, New Delhi-110012, India*
[3] *Department of Biotechnology, TERI School of Advanced studies, New Delhi 110070, India*
[4] *Department of Chemistry, Indian Institute of Technology Delhi, New Delhi 110016, India*
[5] *Regional Centre of Advanced Technologies and Materials, Faculty of Science, Palacký University Olomouc, Šlechtitelů 27, 783 71 Olomouc, Czech Republic*

Received: 24 February 2020 / **Revised:** 3 October 2020 / **Accepted:** 8 October 2020

ABSTRACT

Recently developed lead-free double perovskite nanocrystals (NCs) have been proposed for the possible application in solution-processed optoelectronic devices. However, the optoelectronic applications of double perovskite NCs have been hampered due to the structural and chemical instability in the presence of polar molecules. Here, we report a facile strategy for the synthesis and purification of $Cs_2AgBiBr_6$ double perovskite NCs that remained stable even after washing with polar solvent. This is realized with our efficient colloidal route to synthesize $Cs_2AgBiBr_6$ NCs that involve stable and strongly coordinated precursor such as silver-trioctylphosphine complex together with bismuth neodecanoate, which leads to a significantly improved chemical and colloidal stability. Using layer-by-layer solid-state ligand exchange technique, a compact and crack-free thin film of $Cs_2AgBiBr_6$ NCs were fabricated. Finally, perovskite solar cells consisting of $Cs_2AgBiBr_6$ as an absorber layer were fabricated and tested.

KEYWORDS

double perovskite nanocrystals, colloidal and chemical stability, thin film, solar cells

1 Introduction

Solution-processed solar cells based on lead halide perovskite have already achieved record certified efficiency over 22% in a single-junction architecture [1]. The outstanding device performance of lead-based perovskite is attributed to the remarkable optical and electronic properties including narrow bandgap with high optical absorption coefficient, long diffusion length and carrier lifetime, defect tolerant nature, balanced charge carrier transport and low exciton binding energies [2]. Despite remarkable progress and outstanding performance, the practical utilization of this fastest growing photovoltaic technology is hampered by inherent toxicity due to the presence of lead atom and instability in the normal operating conditions such as heat, light and humidity [3]. To overcome such serious issues, the search of stable lead-free perovskite materials is still in progress. In a previous year, extensive computational and experimental research has been carried towards stable and less toxic perovskite materials including Pb replacement either by homovalent elements (Sn, Ge) or hetrovalent elements (Sb, Bi) [4–10]. Indeed, Sn or Ge based perovskite which possesses direct and relatively narrower bandgap could become a nontoxic alternative. Unfortunately, the Sn-based perovskite suffers phase instability due to oxidation of Sn^{2+} into thermodynamically stable Sn^{4+} states [11]. On the other hand perovskite structures based on trivalent element such as Bi or Sb demonstrated undesired optical and electronic properties owing to their reduced electronic dimensionality which make them inappropriate for high-performance optoelectronic applications [9, 10, 12].

Recently, a new class of metal halide perovskite that can be obtained by combination of monovalent metal (M^+ = Na^+, Ag^+) and trivalent metal (M^{3+} = Bi^{3+}, Sb^{3+}, In^{3+}) with general formula $A_2M^+M^{3+}X_6$ (where A = Cs^+ and X = Cl^-, Br^-, I^-) also known as double perovskite (DP), received tremendous computational and experimental research interest as they offer a stable lead-free alternative with nearly preserved three-dimensional (3D) perovskite structures [13–18]. Among a wide range of DP materials, $Cs_2AgBiBr_6$ is the only example that has been successfully incorporated in the photovoltaic devices and became famous in a short period of investigation. The relatively narrow bandgap (1.98–2.3 eV), superior stability in the ambient environment, high optical absorption coefficient and long carrier lifetime make this material promising alternative towards stable and lead-free photovoltaic technology [13, 14, 19]. So far, few articles have been reported on the fabrication of solar cells utilizing $Cs_2AgBiBr_6$ as a light-absorbing material. The perovskite solar cells (PSC) based on $Cs_2AgBiBr_6$ in mesoporous structures with power conversion efficiency (PCE), ~ 2.4% have been first

Address correspondence to ritu@nplindia.org

demonstrated by Greul et al. Nevertheless, the reported device characteristics was suffered from huge hysteresis effect, which was mainly due to the poor morphology of DP films [20]. Since then significant effort has been made to improve the device performance of $Cs_2AgBiBr_6$ based PSCs by utilizing various thin film deposition techniques and device structures [19, 21–25]. Recently, Yang et al. demonstrated enhanced performance of $Cs_2AgBiBr_6$ based PSC by incorporating N719 dye as an interface layer with PCE of 2.84%, which is the highest reported efficiency of $Cs_2AgBiBr_6$ based solar cell so far [26]. Despite the significant effort, device performance is likely to be limited by difficulties in the preparation of high-quality and phase pure films due to the poor solubility of metal precursors in the common organic solvent [21, 27]. Moreover, the phase pure and crystalline thin films of DP materials rely on the high temperature (~ 250 °C) annealing process which is not suitable for flexible optoelectronic applications [20]. In this context, colloidal synthesis of DP NCs that can be subsequently deposited into a thin film by simple solution-based techniques could become an attractive strategy. Recently, significant effort has been made towards the development of various DP NCs [28–38]. Unfortunately, best of our knowledge the optoelectronic applications of any type of DP NCs have not been reported, presumably due to the difficulties in the assembly of colloidal DP NCs into the compact and conductive NCs thin film with desired thickness. Colloidal synthesis of NCs generally utilize long organic ligands such as oleic acid and/or oleylamine that not only control the nucleation and growth during the reaction, also passivate the surface defect and provide colloidal stability [39, 40]. However, excessive ligands act as an insulating barrier, which leads to the poor charge transport through NCs network [41, 42]. Thus, a controlled surface passivation of NCs is necessary to obtain efficient charge transport and good device performance. Therefore, extraction and purification of nanocrystals from the crude solution which also contains unreacted precursors and excessive ligands are very essential for the use of NCs in the thin film devices. The excessive ligands and unreacted precursors in the crude solution is generally removed by antisolvent washing treatment. In comparison to the chalcogenide-based NCs, due to the ionic nature, perovskite NCs are highly sensitive to common polar solvents and readily decompose into non-perovskite phase, therefore the purification of perovskite NCs from crude solution is somehow challenging [28, 40]. Recently, Swarnkar et al. reported that $CsPbI_3$ NCs can be successfully extracted from crude solution by antisolvent precipitation approach using methyl acetate as an antisolvent, but it is still a big challenge to find purification technique for newly developed DP NCs by using suitable solvents [43]. Moreover, the conductive NCs thin film usually fabricated from spin or dip coating techniques followed by ligand exchange with short chain molecules and a layer-by-layer (LBL) approach is often used to achieve the desired thickness of NCs film [44]. However, the reported ligand exchange protocol generally utilizes polar solvents which are not suitable for the existing DP NCs. Therefore, the advance synthetic approach for the stable DP NCs is highly desirable that can be sustained against the polar solvents during the washing and ligand exchange process.

In this report, we demonstrate a new strategy for the synthesis of high-quality and phase pure $Cs_2AgBiBr_6$ DP NCs with enhanced chemical and colloidal stability that utilizing silver-trioctylphosphine complex and commercially available bismuth neodecanoate as the metal precursors. The DP NCs were successfully extracted from crude solution through antisolvent washing method by using isopropanol. The purified DP NCs remained stable in both solution and thin film even in ambient atmosphere that allows us for their use in thin film devices. Using layer-by-layer solid state ligand exchange protocol, highly uniform and crack-free thin film of DP NCs with desired thickness were fabricated and characterized. The optical and electronic properties of DP NCs thin film were determined by ultraviolet–visible (UV–Vis) spectroscopy and ultraviolet photoemission spectroscopy. Finally, solar cells based on DP NCs as an absorbing layer were fabricated and tested.

2 Results and discussion

$Cs_2AgBiBr_6$ NCs were synthesized by hot injection method under an inert atmosphere using standard Schlenk line apparatus. First, 1 mmol $AgNO_3$ was dissolved in 1 mL trioctylphosphine (TOP) by stirring at room temperature for overnight inside nitrogen filled glove box which resulted in clear and transparent solution. Similar to the previous reports [45, 46] where indium and lead atom strongly coordinated with TOP, the high solubility of $AgNO_3$ in TOP is attributed to the strong interaction between silver ion and TOP which resulted stable and strongly coordinated Ag-TOP complex. In brief, a mixture of cesium carbonate and bismuth neodecanoate together with oleic acid, oleylamine and octadecene were first degassed at 110 °C with a continuous supply of argon gas. Once after precursors were fully dissolved, a pre-mixed solution of $AgNO_3$ in trioctylphosphine (Ag-TOP) was injected into the hot mixture of cesium and bismuth precursors. Finally, benzoyl bromide was swiftly injected into the hot reaction mixture resulting prompt color change from pale yellow to orange, indicating the formation of $Cs_2AgBiBr_6$ NCs (see Fig. S1 in the Electronic Supplementary Material (ESM)). The schematic representation of the synthesis process is illustrated in Fig. 1. The detail experimental procedure is discussed in the experimental section. Distinct from the previously reported methods that resulted in immediate precipitation of NCs from the solution [28, 47] our as-synthesized NCs remained stable and optically clear for a longer time, indicating that our synthetic method provides enhanced colloidal stability. After a month of storage in ambient conditions, only a slight yellow precipitate was observed at the bottom of the centrifuge tube. Furthermore, as-synthesized NCs were successfully extracted from crude solution through antisolvent washing treatment

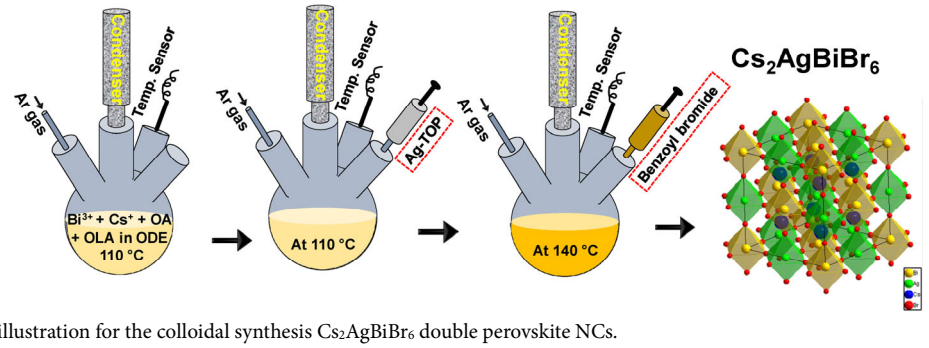

Figure 1 Schematic illustration for the colloidal synthesis $Cs_2AgBiBr_6$ double perovskite NCs.

using isopropanol, which is a very important step to remove the excess ligands and unreacted precursors for further uses and characterizations. Previous report [28] suggested that the extraction of DP NCs from the crude solution somehow challenging as they immediately decomposed when exposes to commonly used antisolvent such as alcohol, acetone and ethyl acetate. Interestingly, our purified NCs remained well dispersed in common nonpolar organic solvent, indicating improved colloidal stability that can be ascribed to the effective surface passivation of NCs by TOP ligand together with oleic acid and oleylamine. We believe that the synthesis of high-quality and stable NCs indeed enabled by the utilization of strongly coordinated silver-trioctylphosphine complex together with benzoyl bromide which act as highly reactive precursors. Previous results also suggested that TOP based synthesis of lead halide perovskite NCs provides remarkable optical properties with enhanced stability [46, 48, 49]. Manna and co-workers explained the reaction mechanism for the synthesis of halide perovskite NCs by using benzoyl halides as halide precursor sources [50]. Where benzoyl bromide shows strong reactivity towards nucleophilic molecules i.e. oleic acid and oleylamine and from esters and amide, respectively (see Eqs. (1) and (2)). The hydrobromic acid also releases during the reaction, which provides highly reactive bromide ions precursor for the nucleation and growth of NCs.

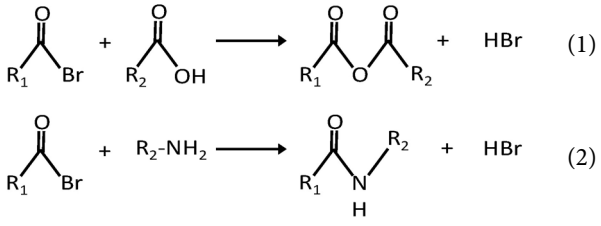

The size and shape of $Cs_2AgBiBr_6$ NCs were analyzed by transmission electron microscopy (TEM). A representative low magnification TEM image of purified NCs with size distribution histogram is shown in Fig. 2(a), displaying narrow size distribution with an average size of 7.6 ± 0.8 nm. The high magnification TEM image is shown in Fig. 2(b), where the well-defined cubic shape of DP NCs without any sign of aggregation are clearly visible that further confirming excellent phase and colloidal stability even after washing with antisolvent. High-resolution TEM image is presented in Fig. 2(c) showing well defined lattice fringes of highly crystalline NCs. The lattice spacing of 0.29 nm associated with the (004) plane of the cubic $Cs_2AgBiBr_6$ NCs. The crystal structure and phase purity of DP NCs were investigated by X-ray diffraction analysis. The X-ray diffraction (XRD) pattern of purified NCs film shown in Fig. 3 had been prepared by drop casting the concentrated NCs dispersion on the glass substrate. The XRD pattern of DP NCs matched well with the calculated cubic double perovskite structures which belong to $Fm\bar{3}m$ space group reported previously [13]. Interestingly, the XRD patterns of NCs film did not contain any side phase impurity even after antisolvent purification steps, indicating excellent phase stability. The selected area electron diffraction pattern (SAED) (Fig. 2(d)) further confirms the cubic phase of DP NCs as ring patterns were well indexed with the cubic double perovskite structure.

It is well established that the formation of desired phase quaternary double perovskite structures requires precise control of reaction reagents and reaction temperature [28, 30, 33]. The significant variations in reaction conditions such as precursors molar ratio, amount of ligands and reaction temperature leads to the formation of undesired phase along with DP structures [51]. Reaction performed with increasing concentration of

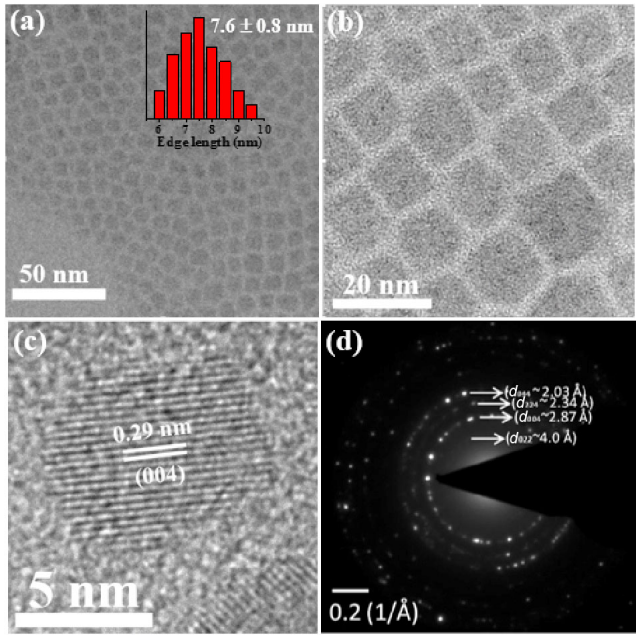

Figure 2 TEM micrographs of purified $Cs_2AgBiBr_6$ NCs. (a) Low-magnification TEM with size distribution histogram that were represented by measuring edge length of nearly 100 NCs. (b) High-magnification TEM micrograph, displaying cubic shape of NCs. (c) HRTEM micrograph of $Cs_2AgBiBr_6$ NCs, lattice spacing of 0.29 nm associated with (004) plane of $Cs_2AgBiBr_6$ NCs. (d) Corresponding SAED patterns of the $Cs_2AgBiBr_6$ NCs.

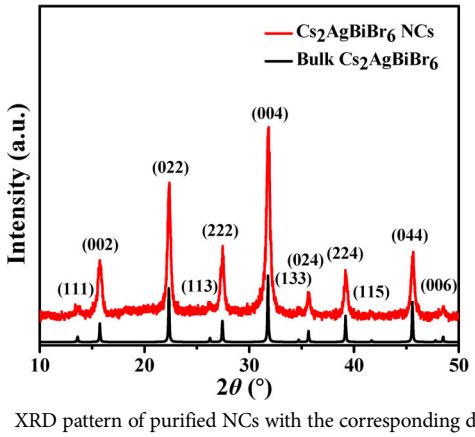

Figure 3 XRD pattern of purified NCs with the corresponding diffraction pattern of bulk $Cs_2AgBiBr_6$.

oleylamine (0.5 mL), produced identical size DP NCs along with an undesired impurity phase which can be assigned to $Cs_3Bi_2Br_9$ and AgBr (Figs. S2(a) and S2(b) in the ESM). However, raising the injection temperature to 170 °C leads to the formation of bigger NCs with broader size distribution accompanied by the formation of small side phase impurity (Figs. S3 and S4 in the ESM).

The optical study of $Cs_2AgBiBr_6$ DP NCs were performed by steady state absorption and photoluminescence spectroscopy. The photograph of purified DP NCs dispersed in toluene is presented in the inset of Fig. 4(a), showing characteristics yellow color of $Cs_2AgBiBr_6$ NCs. The absorption spectrum of NCs is shown in Fig. 4(a), which exhibit sharp absorption peaks centered at 428 nm with the long absorption tail approaching near to 700 nm. The intense absorption peak centered at 428 nm can be attributed to the Bi direct s-p transition, while the presence of long absorption tail up to longer wavelength indicates an indirect nature of DP NCs [29]. The absorption spectra of DP NCs thin-film shares the same absorption profile

as observed in solution, except that Bi s-p transition appeared at 436 nm which was slightly shifted to higher wavelength compared to the absorption obtained in solution. The optical band gap of DP NCs was obtained from Tauc plots shown in Fig. 4(b). Considering indirect transition, the bandgap value of 2.28 eV was estimated, which is close to the values reported for the bulk $Cs_2AgBiBr_6$ [19, 52]. The PL spectra shown in Fig. 4(c) display several characteristic features, dual PL peak with long tails approaching near to 700 nm. The PL spectra can be split into three Gaussian peaks centered at 538, 572, and 619 nm corresponding to the energy of 2.3, 2.16 and 2 eV, respectively. Interestingly, the PL peak located at 2.3 and 2.16 eV have a comparable intensity and the energy difference between these two peaks is only 0.14 eV which is close to the energy difference between calculated indirect and direct bandgap [52]. Moreover, the emission line width for PL peak located at 2.3 eV is much narrower (FWHM 34 nm) than the emission peak centered at 2.16 eV (64 nm). Recently, the PL spectrum of 0D $Cs_3Bi_2X_9$ NCs with dual peak features at room temperature has been reported by Mohammed et al. [53]. The authors suggested that two distinguish PL peak has been attributed to the simultaneous indirect and direct bandgap transitions. Thus on the basis of previous reports and above discussion, we believe that PL peak located at 2.3 eV likely originated from direct bandgap transition whereas PL peak centered at 2.16 eV attributed to the radiative recombination from phonon-assisted indirect transition. The band-edge emission for $Cs_2AgBiBr_6$ DP material either in bulk or NCs is unusual and never been reported. According to previous reports [28, 29, 37]. $Cs_2AgBiBr_6$ DP material shows broad PL emission (FWHM 100–200 nm) with a large stoke shift indicates emission mainly originate from a defect or surface-related states. Our synthetic approach

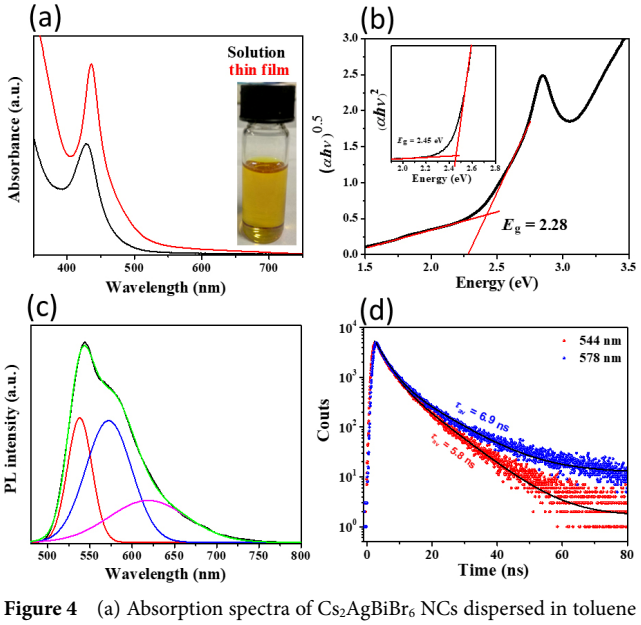

Figure 4 (a) Absorption spectra of $Cs_2AgBiBr_6$ NCs dispersed in toluene (black) and thin film (red) deposited on glass substrate. Photograph of NCs dispersion in toluene showing characteristic yellow color presented in the inset. (b) Tauc plot assuming an indirect transition of $Cs_2AgBiBr_6$ NCs thin film deposited on glass substrate gives an indirect band gap of 2.28 eV. The inset shows Tauc plot for direct transition, intercept of linear fit to the energy axis gives the direct band gap value of 2.43 eV. (c) PL spectra of $Cs_2AgBiBr_6$ NCs dispersion in toluene. Samples were excited using Xenon lamp at 450 nm. Deconvolution of the PL spectrum gives three distinct peaks located at 538, 572, and 619 nm. (d) Time-resolved PL spectra of $Cs_2AgBiBr_6$ NCs collected for direct and indirect emission. The black solid lines in the decay profiles are the two-exponential fits for decays collected for direct and indirect transition respectively.

provides remarkable improvement in optical properties, presumably because of effective surface state passivation.

Figure 4(d) shows the TRPL spectra of $Cs_2AgBiBr_6$ NCs detected at two different emission wavelengths 544 and 578 nm, respectively. Both PL decay curves fitted well by biexponential function (Eq. (3)) with initial fast decay (τ_1) followed by slow decay component (τ_2). In particular, for the decay profile collected at 544 nm, initial fast decay channel has lifetime (τ_1) of 2.9 ns with contribution (α_1) of 75%, while the lifetime of slow decay (τ_2) found to be 8.7 ns with contribution (α_2) of 25%. The average lifetime were calculated from the expression for average lifetime, $\tau_{av} = \Sigma\alpha_i\tau_i^2 / \Sigma\alpha_i\tau_i$ which gives the value of 5.8 ns. On the other hand, for the decay profile collected at 578 nm, initial fast decay channel has lifetime (τ_1) of 3 ns with contribution (α_1) of 77%, while the lifetime of slow decay (τ_2) found to be 10.7 ns with contribution (α_2) of 23% with average lifetime value of 6.9 ns. The fast decay component likely originated from the recombination from surface-related defects, while longer lifetime component was attributed to the intrinsic charge carrier recombination [19]. The lifetimes and contribution of surface related recombination in both direct and indirect transition almost remain same except the lifetime of intrinsic charge carrier recombination for phonon assisted indirect transition is significantly higher than direct transition. These results are in agreement with the previous reports where an indirect transition usually exhibits a longer lifetime than a direct transition [53, 54].

$$I(t) = \alpha_1 \exp\left(\frac{-t}{\tau_1}\right) + \alpha_2 \exp\left(\frac{-t}{\tau_2}\right) \quad (3)$$

Colloidal stability of a purified NCs is highly desirable for the application in optoelectronic devices. To evaluate the colloidal stability of the purified NCs, we have performed UV–Vis absorption characterization of the purified NCs (Figs. S5(a) and S5(b) in the ESM) after long-term storage (30 days) under ambient conditions. We did not observe any significant change in the absorption peak except slight decrease (~ 7%) in the optical density when toluene dispersion of NCs were kept at least for 30 days in ambient conditions. In order to exploit the DP NCs in the solar cell devices, a layer-by-layer spin coating technique was employed for the fabrication of electronic conductive NCs film. The exchange of the long-chain insulating organic ligands with short molecules is necessary to achieve efficient charge transport through the NCs network. The LBL deposition technique not only replace the bulky insulating ligands but also pave the way for the deposition of another layer to achieve the desired thickness of the film. Inspired by previous studies on chalcogenide NCs [44, 55–58], a solid-state ligand exchange (see Experimental Section for detail method) was employed by treating NCs films with tetrabutylammonium bromide (TBAB). Figure 5(a) shows a schematic diagram depicting the layer-by-layer process of NCs assembly into a thin film. In brief, toluene solution of $Cs_2AgBiBr_6$ NCs was first deposited on desired substrate by spin coating. The solid-state ligand exchange was performed by treating NCs film with TBAB solution in isopropanol followed by two consecutive washing steps with isopropanol and toluene to remove the excess ligands. This process was repeated several times to obtain the desired thickness of uniform and shiny yellow film. Since the NCs were not washed away during the cleaning steps and/or deposition of another NCs layers, which clearly indicated that the native ligands on the NCs at least partly or fully exchanged to TBAB molecules. The FTIR spectroscopy was frequently used to identify the adsorbed organic species at the surface of NCs. In the FTIR spectrum (Fig. 5(b)) untreated NCs are

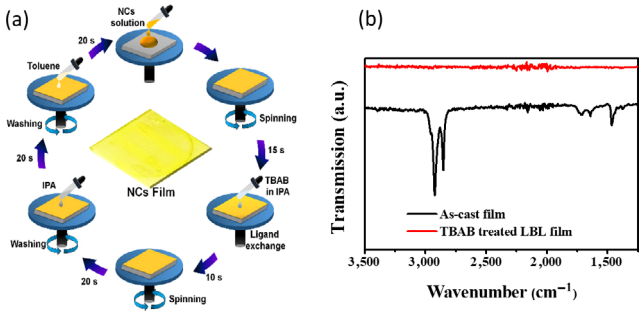

Figure 5 (a) Schematic illustration of layer-by-layer deposition process. (b) FTIR spectra of untreated $Cs_2AgBiBr_6$ NCs film (black curve) and TBAB treated LBL deposited film (red curve).

surrounded by TOP, oleylammonium and oleate ligands, which have a strong C–H stretching vibration peak around 2,800–3,000 cm^{-1} and below 2,000 cm^{-1} [43, 59]. After ligand exchange with TBAB, the C–H stretching peaks were completely vanished and could not be detected in the FTIR spectrum, which indicates that the native ligands were completely replaced by an inorganic ligand of Br^- ions. Similar kinds of complete ligand exchange were also observed by Jeon et al. in the TBAB treated Ag NCs film [58]. According to the previous reports, in case of alkylammonium halide ligands, halide anions bind to surface atoms on the NCs surface and are covered by alkylammonium countercations [58, 60]. The detection of adsorbed organic residue such as alkylammonium cations by FTIR is challenging due to either they can be easily washed out during cleaning steps or could be present in a very little amount which can be below detection limit. Moreover, it is reported that thermal annealing process which is necessary to remove the solvent residues, also effectively remove the organic residue such as alkylammonium counterions [60].

X-ray photoelectron spectroscopy (XPS) was carried out to further investigate the chemical composition and oxidation states of elements in the $Cs_2AgBiBr_6$ NCs. XPS measurement of TBAB treated $Cs_2AgBiBr_6$ NCs film confirms the presence of all constitute elements. The high-resolution core level XPS spectra of Cs 3d, Ag 3d, Bi 4f and Br 3d are shown in Figs. S6(a)–S6(d) in the ESM, respectively. The XPS spectrum (Fig. S6(b) in the ESM) of Ag 3d displays two peaks centered at 367.7 and 373.9 eV, that corresponded to the Ag $3d_{5/2}$ and Ag $3d_{3/2}$ peaks of Ag^+ ions, respectively. Similarly, Fig. S6(c) in the ESM represents the core level XPS spectra of Bi 4f, and displays two distinct peaks centered at 158.3 and 163.8, that belonging to the Bi $4f_{7/2}$ and Bi $4f_{5/2}$ peaks of Bi^{3+} ions, respectively.

The morphology of solution-processed NCs thin film substantially determines the performance of optoelectronic devices. Device performance of NCs based solar cells relies on the smooth, compact and uniform surface as they minimize the carrier recombination at the interfaces and ultimately improve the charge collection efficiency at the electrodes. The morphology of LBL deposited $Cs_2AgBiBr_6$ DP NCs thin film was investigated by atomic force microscopy (AFM) and scanning electron microscopy (SEM). The photograph of NCs film is presented in the inset of Fig. 6(a), showing very smooth and shiny yellow appearance without any visible pinholes on the surface. The AFM morphology shown in Fig. 6(a) display smooth, compact and full coverage of NCs grains with root mean square roughness of 7.5 nm which is free from pinholes and cracks. The high-magnification AFM morphology (Fig. 6(b)) of the film shows uniform grains of DP NCs with an average size of 90–110 nm. The low and high-magnification SEM images in Figs. 6(c) and 6(d) also confirm the uniform and compact assembly of DP NCs throughout the film without any

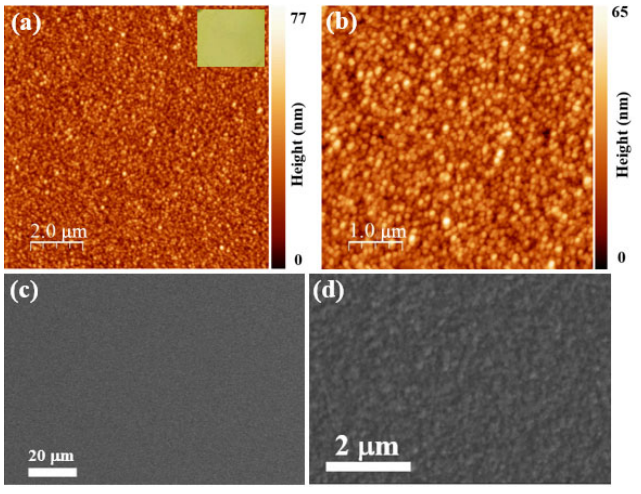

Figure 6 Morphology of TBAB treated LBL deposited films. Tapping mode AFM morphology. (a) Low-magnification AFM image. Inset shows the photograph of LBL deposited film. (b) High-magnification AFM image, demonstrating crack-free and compact assembly of NCs. (c) Low- and (d) high-magnification SEM morphology, respectively displaying similar features observed in AFM images.

sign of aggregation.

The absorption spectra (Fig. S7(a) in the ESM) of TBAB treated NCs film display similar features like the untreated film. Both treated and untreated film consist of sharp absorption peak at 437 and 436 nm, respectively, with long tails approaches near 700 nm that indicates indirect nature of bandgap. Interestingly, the impurity absorption peak at 380 nm which was assigned to the isolated octahedral $BiBr_6^{3-}$ complex was not detected in any kind of film [29, 31]. These results indicate that $Cs_2AgBiBr_6$ films are stable even after ligand exchange treatment. Bandgap with the position of valence and conduction band of $Cs_2AgBiBr_6$ NCs are essential parameters for their application in solar cell devices. The optical bandgap of TBAB treated NCs film was obtained from Tauc plots presented in Fig. S7(b) in the ESM. Considering the indirect transition, bandgap value of 2.27 eV was calculated, which is similar to the untreated film. Position of the valence band (VB) and conduction band (CB) energy with respect to vacuum level was calculated by ultraviolet photoemission spectroscopy (UPS) according to the previously reported methods [59, 61, 62]. The detail method for UPS measurement and extracted parameters are given in Figs. S8(a)–S8(c) in the ESM. The VB and CB of the TBAB treated $Cs_2AgBiBr_6$ NCs film is located at 6.0 and 3.73 eV, respectively, which is close to the reported values [19].

In order to demonstrate the feasibility of $Cs_2AgBiBr_6$ DP NCs in photovoltaic application, a planar heterojunction solar cell in n-i-p architecture has been fabricated (see Experimental Section for details procedure). The schematic of device structure and the corresponding flat band energy level diagram are shown in Figs. 7(a) and 7(b), respectively. The energy level positions of $Cs_2AgBiBr_6$ NCs presented in energy level diagram was calculated by optical and UPS measurement discussed in the previous section. The $Cs_2AgBiBr_6$ NCs absorber layer is sandwiched between the compact TiO_2 and 2,2′,7,7′ tetrakis (N,N-dipmethoxyphenylamine)-9,9′-spirobifluorene (spiro-OMeTAD) as the electron and hole transport material, respectively. The current density–voltage (J–V) characteristics of DP NCs based solar cells in dark and under AM 1.5G illumination conditions with an illumination intensity of 100 mW/cm^2 are shown in Fig. 7(c) that clearly represent well-defined diode characteristics of the device in the chosen n-i-p architecture.

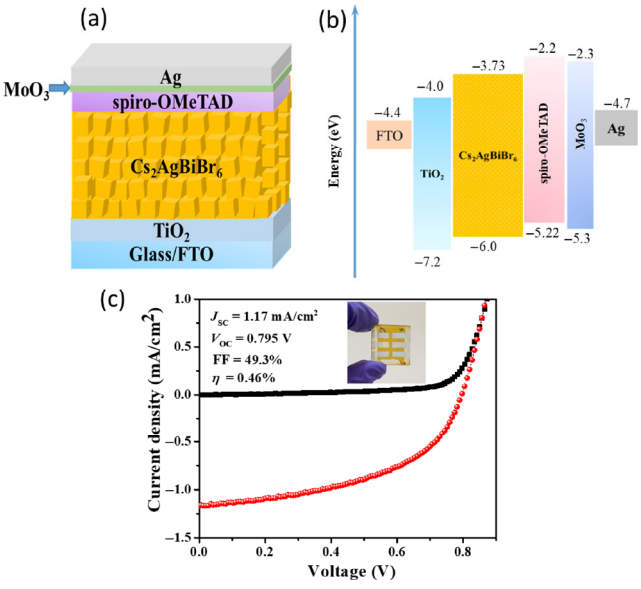

Figure 7 (a) Schematic of n-i-p device structure: FTO/TiO_2/$Cs_2AgBiBr_6$/spiro-OMeTAD/MoO_3/Ag. (b) Corresponding flat band energy level diagram of the perovskite solar cells. (c) Current density–voltage (J–V) characteristics of the perovskite solar cell utilizing $Cs_2AgBiBr_6$ NCs as an absorber layer, under AM 1.5 G condition with an illumination intensity of 100 mW/cm^2.

The best performing device exhibits a short-circuit current density (J_{SC}) of 1.17 mA/cm^2, an open circuit voltage (V_{OC}) of 0.79 V, and a fill factor (FF) of 49.3%, which results in a power conversion efficiency (PCE) of 0.46%. However, the obtained device performance is fairly low compared with the reported PCE values ranging between 0.82% to 2.84% for the bulk $Cs_2AgBiBr_6$ based solar cells [20, 24–26]. The poor device performance of this kind of DP material likely originated to the inherent limitations such as less suitable optical and electronic properties. Moreover, the limited performance of DP NCs based solar cells mainly arises due to the low value of short circuit current density and fill factor that can be originated from several factors such as low charge carrier mobility and large trap density that ultimately resulted in the trap assisted recombination and poor charge collections at the interfaces. Moreover, we have also fabricated solar cells by using larger size NCs synthesized at 170 °C. The current density–voltage (J–V) curves (Fig. S9 in the ESM) showed an open-circuit voltage (V_{OC}) of 0.65 V, a short-circuit current density (J_{SC}) of 0.1 mA/cm^2, a fill factor (FF) of 38.4% and 0.028% PCE for a 0.08 cm^2 cell. The low efficiency of solar cell fabricated with larger size NCs compared to the solar cell those fabricated with optimized NCs indeed attributed to the poor morphology of larger NCs film. SEM image (Fig. S10 in the ESM) of TBAB treated larger NCs film shows clustering with large numbers of cracks appears in the whole thin film. The poorly capped larger and polydisperse NCs might be partially washed out during cleaning step of ligand exchange process which resulted in poor morphology of NCs film. Moreover, when metal/hole transport layer have been deposited on the NCs thin film, large cracks and inhomogeneous morphology may result in more interface defects, which increase the interface carrier recombination and resulted in low J_{SC} and poor device performance. These results indicate that high-quality compact and crack-free thin-film is necessary to obtain the good device performance which can be subsequently deposited from highly stable NCs that can be sustained during washing with polar solvent. Further research work should focus on optimizing ligand exchange process by suitable ligands that provide effective surface states passivation in order to minimize the trap assisted recombination and charge transport layers to enhance the photovoltaic performance. Furthermore, the stability of best performing device fabricated with $Cs_2AgBiBr_6$ NCs synthesized at 140 °C was further investigated. The device retains 85% of its original PCE when kept in ambient conditions without encapsulation over a period of 10 days (Fig. S11 in the ESM), showing huge potential of $Cs_2AgBiBr_6$ NCs based PSCs for long-term stability.

3 Conclusions

In summary, we have demonstrated facile synthesis of $Cs_2AgBiBr_6$ DP NCs with enhanced chemical and colloidal stability. The DP NCs can be readily extracted from crude solution through antisolvent washing method by using isopropanol. The purified DP NCs remained stable in both solution and thin film even in ambient atmosphere that allows us for their use in thin film devices. Layer-by-layer solid state ligand exchange method successfully produced highly uniform and crack-free thin film of DP NCs. The perovskite solar cells utilizing DP NCs as an absorbing layer were fabricated and tested. We believe that our method for the synthesis of $Cs_2AgBiBr_6$ DP NCs may be further extended to other double perovskite structure in order to improve the chemical stability and for enhancing the optical properties. This will open up new possibilities for further material and device optimization towards lead-free perovskite NCs based optoelectronic devices.

4 Experimental section

4.1 Materials

Bismuth neodecanoate, cesium carbonate (99.99%), 1-octadecene (ODE, 90%), oleic acid (OA, 90%), and trioctylphosphine (TOP, 90%), tetrabutylammonium bromide (TBAB, 98%), Titanium (IV) isopropoxide (97%), were purchased from Sigma Aldrich and used without any further purification. Silver nitrate (99.99%) and oleylamine (OLA, 90%) were purchased from Alfa Aesar.

4.2 Synthesis of $Cs_2AgBiBr_6$ nanocrystals

A mixture of 0.3 mmol bismuth neodecanoate, 0.15 mmol of Cs_2CO_3 and 10 mL of ODE together with 0.5 mL OA and 0.24 mL OLA was loaded in a 50 mL four neck round bottom flask equipped with a reflux condenser and degassed via argon bubbling for 30 min at 110 °C under vigorous stirring. Then 0.3 mL premixed Ag-TOP (0.3 mmol $AgNO_3$) solution was injected into the hot reaction mixture and the solution was kept for another 20 min under continuous argon supply. At this stage, all the precursors were fully dissolved and the solution became optically clear pale yellow. Subsequently, the temperature of the flask was set at 140 °C, then 300 μL of benzoyl bromide (2.54 mmol) was swiftly injected into the hot reaction precursors which resulted in the prompt color change from pale yellow to orange, indicating the formation of $Cs_2AgBiBr_6$ NCs. About within 5 s, the reaction flask was rapidly cooled down in an ice-water bath. The crude solution was centrifuged at 5,000 rpm for 5 min, the precipitated solid was discarded and the yellow-orange supernatant was collected. The $Cs_2AgBiBr_6$ NCs were precipitated by adding 30 mL isopropanol into supernatant solution collected after first centrifugation cycle, and then the resulting mixture was centrifuged at 12,000 rpm for 10 min. The light yellow supernatant was discarded and the precipitated NCs were redispersed in toluene and centrifuged again for 5 min at 4,000 rpm to remove larger aggregates. The resulting supernatant was collected and stored for characterization and

device fabrication.

4.3 Characterizations

The transmission electron microscopic (TEM) images of purified NCs were obtained using a FEI Tecnai G2 F 30 STWIN microscope operating at an accelerating voltage of 300 kV. Samples were prepared by placing 10 ∝ L of the diluted NCs solution dispersed in toluene on a carbon-coated copper grid and the samples were dried naturally in the air. The average size of NCs was calculated by measuring the edge length of nearly 100 nanocrystals. The crystal structures of $Cs_2AgBiBr_6$ NCs were obtained by powder XRD using a Rigaku diffractometer equipped with Cu-K_α radiation source (λ = 1.54056 A°). Samples were prepared by dropping the concentrated dispersions of purified NCs on the glass substrate and allowing the solvent to evaporate naturally in air. The absorption spectra were obtained using Shimadzu 2401 PC UV–Vis spectrophotometer. The PL spectra of NCs dispersed in toluene were recorded with a Fluorolog (Jobin Yvon-Horiba, model-3-11) spectrophotometer. The samples were excited with 450 nm incident wavelength of the xenon lamp. The excitation slit width was set at 10 nm and the emission slit width was set at 5 nm. Time-resolved PL spectra were collected using time-correlated single-photon counting (TCSPC) based Fluorolog (Jobin Yvon-Horiba, model-3-11) spectrophotometer. Samples were excited with pulse Nano-LED (λ = 405 nm) with pulse width < 200 ps and pulse repetition rate of 1 MHz. The instrument response function was measured using a non-fluorescence scattering solution in deionized water. The transmission mode of FTIR measurements was performed using a Nicolet 5700 IR spectrometer. For FTIR measurements, NCs films were deposited on the glass substrate by spin coating technique. Surface morphology of LBL deposited NCs thin films were recorded using both atomic force microscopy, AFM Nano First-3100 operated in tapping mode and scanning electron microscopy (SEM, ZEISS AURIGA). The XPS and UPS measurements were performed using a multi-probe surface analysis system (Omicron, Germany). XPS spectra were recorded using a monochromatized AlK_α (1,486.7 eV) radiation sources. UPS spectra were obtained using *in-situ* discharge lamp (OMICRON HIS 13) with He (I) (21.22 eV) radiation source. Electrical characterization was performed using a Keithely-2420 instrument.

4.4 LBL NCs thin film deposition

$Cs_2AgBiBr_6$ NCs thin film was deposited via a layer-by-layer spin coating, using solid-state ligand exchange treatment inside nitrogen-filled glove box. Initially, a layer of NCs was deposited on the desired substrate by dropping 40 µL of NCs solution (~ 20 mg/mL in toluene) followed by spinning at 1,500 rpm for 15 s. Solid-state ligand exchange was performed by dropping 200 µL of TBAB solution (1 mg/mL in IPA) onto NCs layers and allowed to soak for 10 s, followed by spin-coating at 3,000 rpm for 20 s to remove the excess ligand solution. After that, TBAB treated film was first rinsed with IPA and then toluene via spin coating at 3,000 rpm for 20 s each. This process was repeated several times to achieve the desired thickness of shiny yellow and smooth film. Finally, the fabricated film was annealed at 100 °C for 10 min to remove the solvent residue and stored for further characterizations.

4.5 Device fabrication

Solar cells utilizing $Cs_2AgBiBr_6$ NCs as absorber layer with device structure of FTO/TiO_2/$Cs_2AgBiBr_6$/spiro-OMeTAD/MoO_3/Ag were fabricated according to the following procedure. The patterned fluorine-doped tin oxide (FTO) coated glass substrate was sequentially cleaned with detergent, deionized water and acetone in an ultrasonic bath followed by vapors cleaning in boiling isopropanol and then dried in a vacuum oven. The cleaned substrates were treated with UV ozone for 15 min. A 40 nm electron transport layer of compact TiO_2 layer was deposited via a sol-gel method onto UV ozone treated patterned FTO substrate. TiO_2 precursor for the compact TiO_2 layer was prepared by dropwise addition of titanium isopropoxide (0.74 mL) into 8 mL ethanol with vigorous stirring, followed by rapid injection of 60 µL hydrochloric acid into the solution and then the resulting solution was stirred for overnight. The TiO_2 precursor solution was spin-coated on FTO substrates at 2,000 rpm for 20 s and then annealed at 500 °C for 60 min on a hot plate. Subsequently, a ~ 150 nm $Cs_2AgBiBr_6$ NCs absorber layer was deposited on FTO/TiO_2 substrate via LBL spin coating technique described in the previous section. The solution of hole transporting layer (HTL) was prepared by dissolving 72.3 mg of spiro-OMeTAD in 1 mL of chlorobenzene, followed by addition of 8.8 µL of 4-TBP and 17.5 µL of Li-TFSI stock solution (520 mg/mL in acetonitrile). The spiro-OMeTAD hole transporting layer was deposited by spin-coating onto the NCs absorber layer at 5,000 rpm for 30 s. The prepared samples were then transferred into the vacuum deposition chamber. Finally, a 10 nm MoO_3 and a 120 nm thick Ag electrodes were deposited by thermal evaporation through a shadow mask at a rate of 0.1–0.2 and 1–2 Å/s, respectively at a chamber pressure of ~ 10^{-7} Torr. The active area of device was found to be 0.08 cm^2, defined by the shadow mask.

Acknowledgements

The authors are grateful to the Director of the NPL, New Delhi, India for the facility. R. A. gratefully acknowledge the financial support from the Council of Scientific and Industrial Research (CSIR), New Delhi, for the award of RA.

Electronic Supplementary Material: Supplementary material (photographs of reaction solution before and after injection of benzoyl bromide, TEM and XRD pattern of $Cs_2AgBiBr_6$ NCs synthesized using higher concentration of oleylamine, TEM and XRD pattern of $Cs_2AgBiBr_6$ NCs synthesized at 170 °C, UV–Vis absorption spectra and photograph of fresh and aged samples, high-resolution XPS spectra of Cs 3d, Ag 3d, Bi 4f and Br 3d of TBAB treated $Cs_2AgBiBr_6$ NCs film, absorption spectra and Tauc plot of TBAB treated thin film of $Cs_2AgBiBr_6$ NCs, detail method and UPS measurement of TBAB treated $Cs_2AgBiBr_6$ NCs film, *J*–*V* characteristics of solar cell utilizing bigger $Cs_2AgBiBr_6$ NCs synthesized at 170 °C, SEM image of TBAB treated $Cs_2AgBiBr_6$ NCs film synthesized at 170 °C, *J*–*V* curve for aged device) is available in the online version of this article at https://doi.org/10.1007/s12274-020-3161-6.

References

[1] Yang, W. S.; Park, B. W.; Jung, E. H.; Jeon, N. J.; Kim, Y. C.; Lee, D. U.; Shin, S. S.; Seo, J.; Kim, E. K.; Noh, J. H. et al. Iodide management in formamidinium-lead-halide–based perovskite layers for efficient solar cells. *Science* **2017**, *356*, 1376–1379.

[2] Xiao, Z. W.; Song, Z. N.; Yan, Y. F. From lead halide perovskites to lead-free metal halide perovskites and perovskite derivatives. *Adv. Mater*. **2019**, *31*, 1803792.

[3] Yang, Y.; You, J. B. Make perovskite solar cells stable. *Nature* **2017**, *544*, 155–156.

[4] Chung, I.; Song, J. H.; Im, J.; Androulakis, J.; Malliakas, C. D.; Li, H.; Freeman, A. J.; Kenney, J. T.; Kanatzidis, M. G. $CsSnI_3$: Semiconductor or metal? High electrical conductivity and strong near-infrared photoluminescence from a single material. High hole mobility and

phase-transitions. *J. Am. Chem. Soc.* **2012**, *134*, 8579–8587.
[5] Huang, L. Y; Lambrecht, W. R. L. Electronic band structure, phonons, and exciton binding energies of halide perovskites $CsSnCl_3$, $CsSnBr_3$, and $CsSnI_3$. *Phys. Rev. B* **2013**, *88*, 165203.
[6] Chakraborty, S.; Xie, W.; Mathews, N.; Sherburne, M.; Ahuja, R.; Asta, M.; Mhaisalkar, S. G. Rational design: A high-throughput computational screening and experimental validation methodology for lead-free and emergent hybrid perovskites. *ACS Energy Lett.* **2017**, *2*, 837–845.
[7] Liao, W. Q.; Zhao, D. W.; Yu, Y.; Grice, C. R.; Wang, C. L.; Cimaroli, A. J.; Schulz, P.; Meng, W. W.; Zhu, K.; Xiong, R. G. et al. Lead-free inverted planar formamidinium tin triiodide perovskite solar cells achieving power conversion efficiencies up to 6.22%. *Adv. Mater.* **2016**, *28*, 9333–9340.
[8] Gupta, S.; Bendikov, T.; Hodes, G.; Cahen, D. $CsSnBr_3$, a lead-free halide perovskite for long-term solar cell application: Insights on SnF_2 addition. *ACS Energy Lett.* **2016**, *1*, 1028–1033.
[9] Park, B. W.; Philippe, B.; Zhang, X. L.; Rensmo, H.; Boschloo, G.; Johansson, E. M. J. Bismuth based hybrid perovskites $A_3Bi_2I_9$ (A: Methylammonium or cesium) for solar cell application. *Adv. Mater.* **2015**, *27*, 6806–6813.
[10] Saparov, B.; Hong, F.; Sun, J. P.; Duan, H. S.; Meng, W. W.; Cameron, S.; Hill, I. G.; Yan, Y. F.; Mitzi, D. B. Thin-film preparation and characterization of $Cs_3Sb_2I_9$: A lead-free layered perovskite semiconductor. *Chem. Mater.* **2015**, *27*, 5622–5632.
[11] Jellicoe, T. C.; Richter, J. M.; Glass, H. F. J.; Tabachnyk, M.; Brady, R.; Dutton, S. E.; Rao, A.; Friend, R. H.; Credgington, D.; Greenham, N. C. et al. Synthesis and optical properties of lead-free cesium tin halide perovskite nanocrystals. *J. Am. Chem. Soc.* **2016**, *138*, 2941–2944.
[12] Giustino, F.; Snaith, H. J. Toward lead-free perovskite solar cells. *ACS Energy Lett.* **2016**, *1*, 1233–1240.
[13] Slavney, A. H.; Hu, T.; Lindenberg, A. M.; Karunadasa, H. I. A bismuth-halide double perovskite with long carrier recombination lifetime for photovoltaic applications. *J. Am. Chem. Soc.* **2016**, *138*, 2138–2141.
[14] McClure, E. T.; Ball, M. R.; Windl, W.; Woodward, P. M. Cs_2AgBiX_6 (X = Br, Cl): New visible light absorbing, lead-free halide perovskite semiconductors. *Chem. Mater.* **2016**, *28*, 1348–1354.
[15] Volonakis, G.; Filip, M. R.; Haghighirad, A. A.; Sakai, N.; Wenger, B.; Snaith, H. J.; Giustino, F. Lead-free halide double perovskites via heterovalent substitution of noble metals. *J. Phys. Chem. Lett.* **2016**, *7*, 1254–1259.
[16] Savory, C. N.; Walsh, A.; Scanlon, D. O. Can Pb-free halide double perovskites support high-efficiency solar cells? *ACS Energy Lett.* **2016**, *1*, 949–955.
[17] Volonakis, G.; Haghighirad, A. A.; Milot, R. L.; Sio, W. H.; Filip, M. R.; Wenger, B.; Johnston, M. B.; Herz, L. M.; Snaith, H. J.; Giustino, F. $Cs_2InAgCl_6$: A new lead-free halide double perovskite with direct band Gap. *J. Phys. Chem. Lett.* **2017**, *8*, 772–778.
[18] Tran, T. T.; Panella, J. R.; Chamorro, J. R.; Morey, J. R.; McQueen, T. M. Designing indirect–direct bandgap transitions in double perovskites. *Mater. Horiz.* **2017**, *4*, 688–693.
[19] Pantaler, M.; Cho, K. T.; Queloz, V. I. E.; García Benito, I.; Fettkenhauer, C.; Anusca, I.; Nazeeruddin, M. K.; Lupascu, D. C.; Grancini, G. Hysteresis-free lead-free double-perovskite solar cells by interface engineering. *ACS Energy Lett.* **2018**, *3*, 1781–1786.
[20] Greul, E.; Petrus, M. L.; Binek, A.; Docampo, P.; Bein, T. Highly stable, phase pure $Cs_2AgBiBr_6$ double perovskite thin films for optoelectronic applications. *J. Mater. Chem. A* **2017**, *5*, 19972–19981.
[21] Wu, C. C.; Zhang, Q. H.; Liu, Y.; Luo, W.; Guo, X.; Huang, Z. R.; Ting, H.; Sun, W. H.; Zhong, X. R.; Wei, S. Y. et al. The dawn of lead-free perovskite solar cell: Highly stable double perovskite $Cs_2AgBiBr_6$ film. *Adv. Sci.* **2018**, *5*, 1700759.
[22] Ning, W. H.; Wang, F.; Wu, B.; Lu, J.; Yan, Z. B.; Liu, X. J.; Tao, Y. T.; Liu, J. M.; Huang, W.; Fahlman, M. et al. Long electron-hole diffusion length in high-quality lead-free double perovskite films. *Adv. Mater.* **2018**, *30*, 1706246.
[23] Gao, W. Y.; Ran, C. X.; Xi, J.; Jiao, B.; Zhang, W. W.; Wu, M. C.; Hou, X.; Wu, Z. X. High-quality $Cs_2AgBiBr_6$ double perovskite film for lead-free inverted planar heterojunction solar cells with 2.2% efficiency. *ChemPhysChem* **2018**, *19*, 1696–1700.
[24] Kentsch, R.; Scholz, M.; Horn, J.; Schlettwein, D.; Oum, K.; Lenzer, T. Exciton dynamics and electron–phonon coupling affect the photovoltaic performance of the $Cs_2AgBiBr_6$ double perovskite. *J. Phys. Chem. C* **2018**, *122*, 25940–25947.
[25] Igbari, F.; Wang, R.; Wang, Z. K.; Ma, X. J.; Wang, Q.; Wang, K. L.; Zhang, Y.; Liao, L. S.; Yang, Y. Composition stoichiometry of $Cs_2AgBiBr_6$ films for highly efficient lead-free perovskite solar cells. *Nano Lett.* **2019**, *19*, 2066–2073.
[26] Yang, X. Q.; Chen, Y. H.; Liu, P. Y.; Xiang, H. M.; Wang, W.; Ran, R.; Zhou, W.; Shao, Z. P. Simultaneous power conversion efficiency and stability enhancement of $Cs_2AgBiBr_6$ lead-free inorganic perovskite solar cell through adopting a multifunctional dye interlayer. *Adv. Funct. Mater.* **2020**, *30*, 2001557.
[27] Jodlowski, A. D.; Rodríguez-Padrón, D.; Luque, R.; de Miguel, G. Alternative perovskites for photovoltaics. *Adv. Energy Mater.* **2018**, *8*, 1703120.
[28] Creutz, S. E.; Crites, E. N.; De Siena, M. C.; Gamelin, D. R. Colloidal nanocrystals of lead-free double-perovskite (elpasolite) semiconductors: Synthesis and anion exchange to access new materials. *Nano Lett.* **2018**, *18*, 1118–1123.
[29] Bekenstein, Y.; Dahl, J. C.; Huang, J.; Osowiecki, W. T.; Swabeck, J. K.; Chan, E. M.; Yang, P. D.; Alivisatos, A. P. The making and breaking of lead-free double perovskite nanocrystals of cesium silver–bismuth halide compositions. *Nano Lett.* **2018**, *18*, 3502–3508.
[30] Locardi, F.; Cirignano, M.; Baranov, D.; Dang, Z. Y.; Prato, M.; Drago, F.; Ferretti, M.; Pinchetti, V.; Fanciulli, M.; Brovelli, S. et al. Colloidal synthesis of double perovskite $Cs_2AgInCl_6$ and Mn-doped $Cs_2AgInCl_6$ nanocrystals. *J. Am. Chem. Soc.* **2018**, *140*, 12989–12995.
[31] Yang, B.; Hong, F.; Chen, J. S.; Tang, Y. X.; Yang, L.; Sang, Y. B.; Xia, X. S.; Guo, J. W.; He, H. X.; Yang, S. Q. et al. Colloidal synthesis and charge-carrier dynamics of $Cs_2AgSb_{1-y}Bi_yX_6$ (X: Br, Cl; $0 \le y \le 1$) double perovskite nanocrystals. *Angew. Chem., Int. Ed.* **2019**, *58*, 2278–2283.
[32] Lee, W.; Hong, S.; Kim, S. Colloidal synthesis of lead-free silver–indium double-perovskite $Cs_2AgInCl_6$ nanocrystals and their doping with lanthanide ions. *J. Phys. Chem. C* **2019**, *123*, 2665–2672.
[33] Liu, Y.; Jing, Y. Y.; Zhao, J.; Liu, Q. L.; Xia, Z. G. Design optimization of lead-free perovskite $Cs_2AgInCl_6$:Bi nanocrystals with 11.4% photoluminescence quantum yield. *Chem. Mater.* **2019**, *31*, 3333–3339.
[34] Dahl, J. C.; Osowiecki, W. T.; Cai, Y.; Swabeck, J. K.; Bekenstein, Y.; Asta, M.; Chan, E. M.; Alivisatos, A. P. Probing the stability and band gaps of $Cs_2AgInCl_6$ and $Cs_2AgSbCl_6$ lead-free double perovskite nanocrystals. *Chem. Mater.* **2019**, *31*, 3134–3143.
[35] Locardi, F.; Sartori, E.; Buha, J.; Zito, J.; Prato, M.; Pinchetti, V.; Zaffalon, M. L.; Ferretti, M.; Brovelli, S.; Infante, I. et al. Emissive Bi-doped double perovskite $Cs_2Ag_{1-x}Na_xInCl_6$ nanocrystals. *ACS Energy Lett.* **2019**, *4*, 1976–1982.
[36] Lamba, R. S.; Basera, P.; Bhattacharya, S.; Sapra, S. Band gap engineering in $Cs_2(Na_xAg_{1-x})BiCl_6$ double perovskite nanocrystals. *J. Phys. Chem. Lett.* **2019**, *10*, 5173–5181.
[37] Zhou, L.; Xu, Y. F.; Chen, B. X.; Kuang, D. B.; Su, C. Y. Synthesis and photocatalytic application of stable lead-free $Cs_2AgBiBr_6$ perovskite nanocrystals. *Small* **2018**, *14*, 1703762.
[38] Kshirsagar, A. S.; Nag, A. Synthesis and optical properties of colloidal $Cs_2AgSb_{1-x}Bi_xCl_6$ double perovskite nanocrystals. *J. Chem. Phys.* **2019**, *151*, 161101.
[39] Ip, A. H.; Thon, S. M.; Hoogland, S.; Voznyy, O.; Zhitomirsky, D.; Debnath, R.; Levina, L.; Rollny, L. R.; Carey, G. H.; Fischer, A. et al. Hybrid passivated colloidal quantum dot solids. *Nat. Nanotechnol.* **2012**, *7*, 577–582.
[40] Li, J. H.; Xu, L. M.; Wang, T.; Song, J. Z.; Chen, J. W.; Xue, J.; Dong, Y. H.; Cai, B.; Shan, Q. S.; Han, B. N. et al. 50-Fold EQE improvement up to 6.27% of solution-processed all-inorganic perovskite $CsPbBr_3$ QLEDs via surface ligand density control. *Adv. Mater.* **2017**, *29*, 1603885.
[41] Kovalenko, M. V.; Scheele, M.; Talapin, D. V. Colloidal nanocrystals with molecular metal chalcogenide surface ligands. *Science* **2009**, *324*, 1417–1420.
[42] Ahmad, R.; Arora, V.; Srivastava, R.; Sapra, S.; Kamalasanan, M. N. Enhanced performance of organic photovoltaic devices by incorporation of tetrapod-shaped CdSe nanocrystals in polymer-fullerene systems. *Phys. Status Solidi A* **2013**, *210*, 785–790.

[43] Swarnkar, A.; Marshall, A. R.; Sanehira, E. M.; Chernomordik, B. D.; Moore, D. T.; Christians, J. A.; Chakrabarti, T.; Luther, J. M. Quantum dot-induced phase stabilization of α-$CsPbI_3$ perovskite for high-efficiency photovoltaics. *Science* **2016**, *354*, 92–95.

[44] Luther, J. M.; Law, M.; Song, Q.; Perkins, C. L.; Beard, M. C.; Nozik, A. J. Structural, optical, and electrical properties of self-assembled films of PbSe nanocrystals treated with 1,2-ethanedithiol. *ACS Nano* **2008**, *2*, 271–280.

[45] Xu, Z. H.; Li, Y.; Li, J. Z.; Pu, C. D.; Zhou, J. H.; Lv, L. L.; Peng, X. G. Formation of size-tunable and nearly monodisperse InP nanocrystals: Chemical reactions and controlled synthesis. *Chem. Mater*. **2019**, *31*, 5331–5341.

[46] Liu, F.; Zhang, Y. H.; Ding, C.; Kobayashi, S.; Izuishi, T.; Nakazawa, N.; Toyoda, T.; Ohta, T.; Hayase, S.; Minemoto, T. et al. Highly luminescent phase-stable $CsPbI_3$ perovskite quantum dots achieving near 100% absolute photoluminescence quantum yield. *ACS Nano* **2017**, *11*, 10373–10383.

[47] Protesescu, L.; Yakunin, S.; Bodnarchuk, M. I.; Krieg, F.; Caputo, R.; Hendon, C. H.; Yang, R. X.; Walsh, A.; Kovalenko, M. V. Nanocrystals of cesium lead halide perovskites ($CsPbX_3$, X = Cl, Br, and I): Novel optoelectronic materials showing bright emission with wide color gamut. *Nano Lett*. **2015**, *15*, 3692–3696.

[48] Lu, C.; Li, H.; Kolodziejski, K.; Dun, C. C.; Huang, W. X.; Carroll, D.; Geyer, S. M. Enhanced stabilization of inorganic cesium lead triiodide ($CsPbI_3$) perovskite quantum dots with tri-octylphosphine. *Nano Res*. **2018**, *11*, 762–768.

[49] Li, Y.; Wang, X. Y.; Xue, W. N.; Wang, W.; Zhu, W.; Zhao, L. J. Highly luminescent and stable $CsPbBr_3$ perovskite quantum dots modified by phosphine ligands. *Nano Res*. **2019**, *12*, 785–789.

[50] Imran, M.; Caligiuri, V.; Wang, M. J.; Goldoni, L.; Prato, M.; Krahne, R.; De Trizio, L.; Manna, L. Benzoyl halides as alternative precursors for the colloidal synthesis of lead-based halide perovskite nanocrystals. *J. Am. Chem. Soc*. **2018**, *140*, 2656–2664.

[51] Ravi, V. K.; Singhal, N.; Nag, A. Initiation and future prospects of colloidal metal halide double-perovskite nanocrystals: Cs_2AgBiX_6 (X = Cl, Br, I). *J. Mater. Chem. A* **2018**, *6*, 21666–21675.

[52] Steele, J. A.; Puech, P.; Keshavarz, M.; Yang, R. X.; Banerjee, S.; Debroye, E.; Kim, C. W.; Yuan, H. F.; Heo, N. H.; Vanacken, J. et al. Giant electron–phonon coupling and deep conduction band resonance in metal halide double perovskite. *ACS Nano* **2018**, *12*, 8081–8090.

[53] Zhang, Y. H.; Yin, J.; Parida, M. R.; Ahmed, G. H.; Pan, J.; Bakr, O. M.; Brédas, J. L.; Mohammed, O. F. Direct-indirect nature of the bandgap in lead-free perovskite nanocrystals. *J. Phys. Chem. Lett*. **2017**, *8*, 3173–3177.

[54] Hutter, E. M.; Gélvez-Rueda, M. C.; Osherov, A.; Bulović, V.; Grozema, F. C.; Stranks, S. D.; Savenije, T. J. Direct–indirect character of the bandgap in methylammonium lead iodide perovskite. *Nat. Mater*. **2017**, *16*, 115–120.

[55] Tang, J.; Kemp, K. W.; Hoogland, S.; Jeong, K. S.; Liu, H.; Levina, L.; Furukawa, M.; Wang, X. H.; Debnath, R.; Cha, D. et al. Colloidal-quantum-dot photovoltaics using atomic-ligand passivation. *Nat. Mater*. **2011**, *10*, 765–771.

[56] Oh, S. J.; Wang, Z. Q.; Berry, N. E.; Choi, J. H.; Zhao, T. S.; Gaulding, E. A.; Paik, T.; Lai, Y. M.; Murray, C. B.; Kagan, C. R. Engineering charge injection and charge transport for high performance PbSe nanocrystal thin film devices and circuits. *Nano Lett*. **2014**, *14*, 6210–6216.

[57] Bernechea, M.; Miller, N. C.; Xercavins, G.; So, D.; Stavrinadis, A.; Konstantatos, G. Solution-processed solar cells based on environmentally friendly $AgBiS_2$ nanocrystals. *Nat. Photonics* **2016**, *10*, 521–525.

[58] Jeon, S.; Ahn, J.; Kim, H.; Woo, H. K.; Bang, J.; Lee, W. S.; Kim, D.; Hossain, A.; Oh, S. J. Investigation of the chemical effect of solvent during ligand exchange on nanocrystal thin films for wearable sensor applications. *J. Phys. Chem. C* **2019**, *123*, 11001–11010.

[59] Ahmad, R.; Srivastava, R.; Bhardwaj, H.; Yadav, S.; Nand Singh, V.; Chand, S.; Singh, N.; Sapra, S. Size-tunable synthesis of colloidal silver sulfide nanocrystals for solution-processed photovoltaic applications. *ChemistrySelect* **2018**, *3*, 5620–5629.

[60] Ning, Z. J.; Dong, H. P.; Zhang, Q.; Voznyy, O.; Sargent, E. H. Solar cells based on inks of n-type colloidal quantum dots. *ACS Nano* **2014**, *8*, 10321–10327.

[61] Chuang, C. H. M.; Brown, P. R.; Bulović, V.; Bawendi, M. G. Improved performance and stability in quantum dot solar cells through band alignment engineering. *Nat. Mater*. **2014**, *13*, 796–801.

[62] Ahmad, R.; Srivastava, R.; Yadav, S.; Singh, D.; Gupta, G.; Chand, S.; Sapra, S. Functionalized molybdenum disulfide nanosheets for 0D–2D hybrid nanostructures: Photoinduced charge transfer and enhanced photoresponse. *J. Phys. Chem. Lett*. **2017**, *8*, 1729–1738.